Bioactive Materials 20 (2023) 243–258

Contents lists available at ScienceDirect

Bioactive Materials

journal homepage: www.keaipublishing.com/en/journals/bioactive-materials

Blending with transition metals improves bioresorbable zinc as better medical implants

Yingchao Su [a,1], Jiayin Fu [b,c,1], Juncen Zhou [a], Elias Georgas [a], Shaokang Du [d], Yi-Xian Qin [a], Yadong Wang [b], Yufeng Zheng [e], Donghui Zhu [a,*]

[a] Department of Biomedical Engineering, Stony Brook University, Stony Brook, NY, USA
[b] Nancy E. and Peter C. Meinig School of Biomedical Engineering, Cornell University, Ithaca, NY, USA
[c] Department of Cardiology, Sir Run Run Shaw Hospital, Zhejiang University, Hangzhou, Zhejiang, China
[d] Academy for Advanced Interdisciplinary Studies, Peking University, Beijing, China
[e] School of Materials Science and Engineering, Peking University, Beijing, China

ARTICLE INFO

Keywords:
Degradation
Cardiovascular
Orthopedic
Subcutaneous
Antibacterial

ABSTRACT

Zinc (Zn) is a new class of bioresorbable metal that has potential for cardiovascular stent material, orthopedic implants, wound closure devices, etc. However, pure Zn is not ideal for these applications due to its low mechanical strength and localized degradation behavior. Alloying is the most common/effective way to overcome this limitation. Still, the choice of alloying element is crucial to ensure the resulting alloy possesses sufficient mechanical strength, suitable degradation rate, and acceptable biocompatibility. Hereby, we proposed to blend selective transition metals (i.e., vanadium-V, chromium-Cr, and zirconium-Zr) to improve Zn's properties. These selected transition metals have similar properties to Zn and thus are beneficial for the metallurgy process and mechanical property. Furthermore, the biosafety of these elements is of less concern as they all have been used as regulatory approved medical implants or a component of an implant such as Ti6Al4V, CoCr, or Zr-based dental implants. Our study showed the first evidence that blending with transition metals V, Cr, or Zr can improve Zn's properties as bioresorbable medical implants. In addition, three *in vivo* implantation models were explored in rats: subcutaneous, aorta, and femoral implantations, to target the potential clinical applications of bioresorbable Zn implants.

1. Introduction

Bioresorbable implants are designed to provide temporary mechanical support for the injured tissue and degrade appropriately *in vivo* to avoid a removal surgery for medical implant devices. When compared to the other two bioresorbable metals, magnesium (Mg) and iron (Fe), zinc (Zn) is a new class of bioresorbable metal that exhibits a more promising biodegradation behavior to match the clinical requirement [1,2]. As the second most abundant trace mineral in the human body, Zn is pivotal in maintaining cardiac function and stimulating bone formation and mineralization [3]. Therefore, Zn has great potential as new generation cardiovascular stents [1,2,4–6], orthopedic implants [7,8], and wound closure devices [9].

In addition to the favorable biodegradation rate and significant biological roles, Zn possesses a much higher mechanical strength than bioresorbable polymers. However, pure Zn still lacks sufficient mechanical strength for cardiovascular stents and load-bearing orthopedic implants [5]. Furthermore, pure Zn has shown localized degradation in previous studies, which could lead to a high risk of sudden implant failure [1,2,4]. Alloying is the most common but simple and effective way to overcome the limitations of Zn's mechanical and corrosion properties. The choice of blending element is crucial to ensure the resulting alloy possesses sufficient mechanical strength, suitable degradation behavior, and acceptable biocompatibility. Various alloying elements have been explored, including Mg [7,10–13], strontium (Sr) [7,14,15], calcium (Ca) [7,14], lithium (Li) [16,17], and rare earth elements [18,19].

Transition metals are attractive in biomedical applications benefiting

Peer review under responsibility of KeAi Communications Co., Ltd.
* Corresponding author.
E-mail address: Donghui.Zhu@stonybrook.edu (D. Zhu).
[1] These authors contributed equally to this work.

https://doi.org/10.1016/j.bioactmat.2022.05.033
Received 15 February 2022; Received in revised form 27 May 2022; Accepted 27 May 2022

from their good mechanical and chemical properties. Zn, Ti, Fe, and Co have been used as metallic substrates. In contrast, the Vanadium (V), Chromium (Cr), manganese (Mn), copper (Cu), Zirconium (Zr), and silver (Ag) have been blended into the metallic biomaterials [20]. Among them, Mn [21], Ag [22], Fe [23], and Cu [24–26] have been explored previously in Zn alloys. In surveying more alloying possibilities, three transition metallic elements, Cr, Zr, V, have been targeted in the present study because of their similar metallurgy properties to Zn. Specifically, a low atomic percentage of 0.5% were chosen based on the phase diagrams in the Zn–Cr, Zr, V binary system. This atomic percentage is higher than their solid solubilities in Zn and could ensure a certain amount of intermetallic phase precipitated in the metallurgical process [27–29]. In addition, the transition metals could potentially form strong local atomic bonding with Zn based on a first-principle study of their effects on the basal-plane stacking fault energies of Zn alloys [30]. This could potentially be beneficial to improve the mechanical property of Zn materials.

Biosafety is one of the most critical issues to consider when designing these Zn materials. Cr and V are the trace elements in the human body, while Zr is deemed to be nontoxic trace elements with unknown functions [31]. It is noteworthy that biosafety is generally dose dependent. When these elements are used at appropriate concentration ranges, the biosafety is of less concern and could have potential biological benefits. Therefore, in the present study, the biological performances of these Zn binary alloys blended with a low percentage (0.5 at. %) of V, Cr or Zr were explored. Moreover, biodegradation and biological performances, including biosafety of biodegradable materials, depend on the implantation locations. Thus, three *in vivo* locations in rat model were used in the present study: subcutaneous, arterial, and femoral tissues. This could provide a comprehensive evaluation of the novel Zn materials in soft and hard tissues, which could be first-hand evidence of these biodegradable materials in specific biomedical applications, including cardiovascular, wound closure, and orthopedic applications.

2. Experimental section

2.1. Material preparation and microstructure characterization

Zn binary alloys ingots blended with different alloying elements were prepared from pure Zn (99.99%), pure Cr (99.99%), pure Zr (99.99%), and pure V (99.9%) ingots by gravity casting. The casted cylinders were heat-treated at 350 °C for 48 h and water quenched and further extruded at 260 °C from Ø 28 mm to Ø 10 mm. The extruded alloys were labeled as Zn-0.5 V, Zn-0.5Cr, and Zn-0.5Zr alloys. Pure Zn (99.99%) was also extruded as a comparison. All the Zn materials were cut into discs (Ø 10 mm × 5 mm) for *in vitro* tests or drawn to thin wires (Ø 0.25 mm) for *in vivo* tests. The disc samples were polished using #1200 sandpaper, while the wire samples were electropolished using a voltage of 10 V in a mixture of ethanol (885 ml), butanol (100 ml), aluminum chloride hexahydrate ($AlCl_3{\cdot}6H_2O$) (109 g), zinc chloride ($ZnCl_2$) (250 g) and water (120 ml) for 2 min [32]. Zn samples' microstructure and phase composition were characterized using optical microscopy (Olympus BX51 M) and X-ray diffraction (XRD, Rigaku DMAX240), respectively. The XRD was equipped with Cu Ka radiation and operated at 40 kV and 100 mA with the scanning rate and step of 4°/min and 0.02°, respectively.

2.2. Mechanical test

The Zn and its alloys specimens were machined along the extrusion direction for the mechanical test according to ASTM-E8/E8M standards [33]. The test was carried out on a universal material test machine (Instron 5969, USA) at a strain rate of 1×10^{-4} s^{-1}. The yield strength was determined as the stress at which the 0.2% plastic deformation occurred.

2.3. In vitro degradation test

All the degradation tests were carried out in a modified Hanks' solution at 37 ± 0.5 °C as described previously [34–37]. The immersion degradation tests were performed for 1 and 3 months according to a previous study [35]. Briefly, the solution was refreshed every week due to the slow degradation of Zn materials. The pH values of the solution with Zn and its alloys were monitored during the immersion tests. The surface morphologies and phase composition of Zn and its alloys after 1 and 3 months of immersion were characterized using a scanning electron microscope (SEM) and XRD. The CR_w (mm/y) was calculated based on weight loss (W_{loss}, mg) according to the following equation [38]:

$$CR_w = 87.6 \times \frac{W_{loss}}{\rho A t}$$

where ρ is the material density (g/cm^3), t is immersion time (h), A is the sample surface area before the immersion test (cm^2). It is noteworthy that the surface area change over time was not considered.

2.4. Hemocompatibility

The hemolysis and platelet adhesion tests were performed according to the method described previously [8,39]. In brief, healthy human blood (Zen-Bio, US) was diluted by 0.9% sodium chloride solution with a volume ratio of 4:5. Zn and its alloys were pre-treated with 9.8 ml 0.9% sodium chloride solution at 37 °C for 30 min. 0.2 mL diluted blood was then added to each tube and incubated at 37 °C for 60 min. Deionized water and 0.9% sodium chloride solution were incubated with 0.2 mL diluted blood as positive and negative control. After centrifuging at 3000 rpm for 5 min, the supernatants were transferred into 96-well plates and the absorbance (A) was measured by a plate reader (Cytation 5, Biotek, US) at 545 nm. The hemolysis rate (HR) was calculated by the following equation: Hemolysis = $(A_{sample} - A_{negative})/(A_{positive} - A_{negative})$.

Platelet-rich plasma (PRP) (Zen-Bio, US) was used for the platelet adhesion test. 50 μl PRP containing 10^8/μl platelets was overlaid on Zn samples and incubated at 37 °C for 1 h. After gently rinsing with PBS three times to remove the non-adherent platelets, adherent platelets on samples were fixed with 4% paraformaldehyde (PFA, Affymetrix, U.S.) and 2% glutaraldehyde solution (Fisher Chemical, U.S.) at room temperature for 2 h. Samples were then dehydrated with a gradient alcohol solution (30%, 50%, 70%, 90%, and 100%) and hexamethyldisilazane (HMDS) for 10 min, respectively, before they were dried in a desiccator. The samples were sputtered with gold and observed by SEM. At least five different SEM images were selected for counting the number of adherent platelets on each sample.

2.5. Cytocompatibility

Human endothelial cells (EA.hy926, ATCC CRL-2922, US) were cultured in 75 cm^2 flask (BD Bioscience) with Dulbecco's Modified Eagle Medium (DMEM, ATCC, US) containing 10% fetal bovine serum (FBS, ScienCell) and 1% penicillin/streptomycin solution (P/S, ScienCell) [40]. Indirect MTT assay (Thermo Fisher Scientific, US) was used to measure the cell viability with extracts prepared by incubating Zn samples in the culture media at a ratio of 1.25 cm^2/mL for 3 days. The Zn ion concentrations in the collected extracts were measured using a Zn colorimetric assay kit (Bio-Vision, US). The extracts were diluted with culture media to specific concentrations of 25% [41–43]. The cell viability was measured after cultured with the extract solution for 1, 3, and 5 days. Cells with a density of 1×10^5/well were seeded onto each Zn sample in a 24 well plate. After three days of cell culture, the cell morphology was observed by SEM after fixation and dehydration in the same method described above.

2.6. Antibacterial property

Escherichia coli (*E. coli*, ATCC 25922, U.S.) and *Staphylococcus aureus* (*S. aureus*, ATCC 29213, U.S.) were cultured according to the procedures from a previous study [44]. Briefly, the bacteria were cultured in Tryptic Soy Broth (TSB) media at 37 °C and 220 rpm to reach the optical density of 0.5–0.6 at 600 nm. The antibacterial performance was tested with the same procedures from our previous study [41]. 2 ml of the diluted bacterial suspension with a 5 × 105/mL concentration in TSB media was incubated with samples for 24 h at 37 °C and 120 rpm. Diluted bacterial suspension without samples was used as the negative control. The absorbance of the collected bacteria suspension was read at 600 nm. Antibacterial rates in the TSB media were calculated with the following equation: Antibacterial rates = $(A_{negative} - A_{sample})/A_{negative}$. Before the SEM imaging, samples were fixed and dehydrated with the same procedures as described above.

2.7. Animal experiments

To compare different tissue responses on pure Zn and its alloys, samples were implanted into the subcutaneous tissues, the aortas, and the femurs in rats. All procedures were approved by the Cornell University IACUC and Stony Brook University IACUC, following NIH guidelines for the care and use of laboratory animals. Before implantation, samples were sterilized by ultraviolet irradiation for 1 h and subsequently soaked in 70% ethanol for another hour.

2.8. Subcutaneous implantation

The study of subcutaneous implantation adopted young male CD IGS rats (strain code: 001, 8–10 weeks, body weight = 300–325 g, Charles River Laboratories, Boston, MA). Each group of samples was implanted into three different rats (n = 3). Subcutaneous implantation was performed as described previously [45,46]. Briefly, five incisions were made to the subcutaneous tissues of the back and subcutaneous pockets by separating subcutaneous layers with muscle layers. Zn and Zn alloy implants were inserted into separated subcutaneous pockets, and the incisions were closed by absorbable sutures.

2.9. Aortic implantation

Male young CD IGS rats (strain code: 001, 8–10 weeks, body weight = 300–325 g, Charles River Laboratories, Boston, MA) were chosen for the aortic implantation. Each group of samples was implanted into 3 different rats (n = 3). Before implantation, samples were sterilized in 70% ethanol for 1 h for sterilization and then soaked in heparin solution (1 mg/mL in saline) overnight for anticoagulation. Aortic implantation was performed as described previously [2]. Briefly, the midline of the abdominal incision was made to expose the abdominal aorta. The aorta was separated from the inferior vena cava. Blood flow in the aorta was blocked with a microvascular clamp. Zn and Zn alloy wire implants were inserted into the aorta with middle parts (6–8 mm in length) within the lumen and two ends (1–2 mm in length) outside of vessel walls. The microvascular clamp was then removed from the aorta to recover the blood flow. The surgical site was closed with absorbable sutures. No anticoagulation or antiplatelet treatments were administrated pre- or post-operatively.

2.10. Femoral implantation

Male young Sprague Dawley rats (8–10 weeks, body weight = 300–325 g, Taconic Biosciences, NY) were used for the *in vivo* analysis of the femoral implantation, and each group of samples was implanted into 5 different rats (n = 5). Briefly, a 2 cm incision was made longitudinally along the lateral side of the right femur. A cylindrical hole (0.3 mm in diameter) was drilled in the femoral condyle perpendicular to the long axis of the femur. Zn and Zn alloy implants were inserted into the cylindrical hole. The incision was closed in layers with sutures.

2.11. Patency monitoring with ultrasonography

VisualSonics Vevo-2100 High-Resolution Ultrasound was used to monitor blood flow in the abdominal aortas that were implanted with wires in weeks 2, 4, 8, and 12 post-implantations. Animals were anesthetized by isoflurane inhalation (5% for induction and 1.5% for maintenance). The hair on the abdomen areas was removed, and ultrasound gel was applied to the skin before imaging. Ultrasound detector MS 400 was used for ultrasound imaging at 30 MHz. B-mode, color mode, and PW mode images on cross-section planes of the abdomen were acquired. Color mode images determined the patency of the abdominal aorta, and P.W. mode images measured the flow rate in the abdominal aortas.

2.12. X-ray micro-computed tomography (micro-CT)

Three months after implantation, the rats were sacrificed, and the wire implants and the surrounding tissue samples were explanted for analysis. *In vivo* degradation of wire implants was evaluated by high-resolution micro-CT (G.E. eXplore CT-120). The explanted samples were scanned with micro-CT at a resolution of 40 μm/pixel. The volume of each wire was calculated from the 3-dimensional (3D) reconstruction of CT scanning images. *In vivo* degradation rate of wires was calculated based on the wire volume change after 12 weeks of implantations:

$$CR_v = (V_0 - V_t) / At$$

Where V_0 and V_t are the implant volume before and after implantation, A is the initial implant surface area, and t is implantation time (3 months). It is noteworthy that the surface area change over time was not considered.

2.13. Histological analysis

Fixed subcutaneous and aortic tissue were soaked in 30% sucrose solution at 4 °C for 24 h and embedded into the optimal cutting temperature compound (OCT, Sakura Finetek, Torrance, CA), snap-frozen at −80 °C, and cryosectioned at 10 μm. Slides were then stained with hematoxylin and eosin (H&E), Masson's trichrome, and Verhoeff's elastin. Fixed femoral tissue was embedded with polymethyl methacrylate (PMMA) and sectioned at 4 μm. Slides were then stained with Masson Goldner's trichrome and Verhoeff's elastin. All the histological images were captured with a microscope (Eclipse Ti2, Nikon, Japan).

2.14. Immunofluorescence staining

Subcutaneous and aortic tissue sections were first blocked with 1% (in PBS) bovine serum albumin (BSA, Sigma-Aldrich) solution for 30 min and then incubated with the following primary antibodies in 1% BSA solution overnight at 4 °C: CD11b (rabbit polyclonal IgG, PA5-90724, Thermo Fisher Scientific, USA), CD68 (rabbit polyclonal IgG, ab125212, Abcam, USA), CD206 (rabbit polyclonal IgG, ab64693, Abcam, USA), alpha-smooth muscle Actin (αSMA, mouse monoclonal IgG2a, ab7817, Abcam, USA), and endothelial nitric oxide synthase (eNOS, mouse monoclonal IgG1, ab76198, Abcam, USA). After that, samples were washed with PBS and incubated with goat anti-rabbit secondary antibody (Alexa Fluor 594, A-11037, Thermo Fisher Scientific, USA) or goat anti-mouse antibody (Alexa Fluor 488, A-11029, Thermo Fisher Scientific, USA) for 1 h at room temperature. Nuclei were counterstained with 4', 6-diamidino-2-phenylindole (DAPI, Krackeler Scientific, USA). Tissue sections without primary antibody incubation were used as negative controls. The stained samples were imaged with the inverted immunofluorescence microscope (Eclipse Ti2, Nikon,

Japan).

2.15. SEM characterizations

The explanted wires with surrounding subcutaneous or aortic tissue were rinsed with phosphate-buffered saline (PBS, pH 7.2), fixed in 4% paraformaldehyde in PBS at 4 °C for 1 h. For SEM examination, the samples were dehydrated in gradient ethanol (50%, 70%,80%, 90%, and 100%, 10 min for each concentration) and then coated with gold. Tissue coverage on wire surface along long axes and cross-section views was observed with SEM and attached EDS. The explanted wires with surrounding femoral tissue were embedded in PMMA, then polished and gold-coated to observe the cross-sections with SEM and attached EDS. The bone area (BA) and bone-to-implant contact (BIC) were quantified based on at least five cross-sectional SEM images. BA was the ratio of bone area to a total area extending 100 μm from the implant. BIC was calculated by normalizing the implant perimeter directly in contact with bone over the whole perimeter length [47].

2.16. Statistical analysis

All data were presented as mean ± standard deviation. One-way or two-way ANOVA followed by Turkey's post-hoc test was used to analyze the statistical significance. $P < 0.05$ was considered statistically significant.

3. Results

3.1. Microstructure and mechanical property

Optical micrographs, XRD patterns, and the tensile mechanical properties of the extruded Zn and its alloys were characterized (Fig. 1). All the Zn materials showed similar crystal sizes, and all the alloys showed an equiaxed α–Zn phase with uniformly distributed second phases (Fig. 1a). Especially, the Zn-0.5 V alloy exhibited a much finer grain size and second phase structure when compared to the other two alloys. The XRD patterns indicated that all the alloys showed a similar hexagonal close-packed structure with different second phases for different alloys (Fig. 1b). Compared to pure Zn, all the alloys

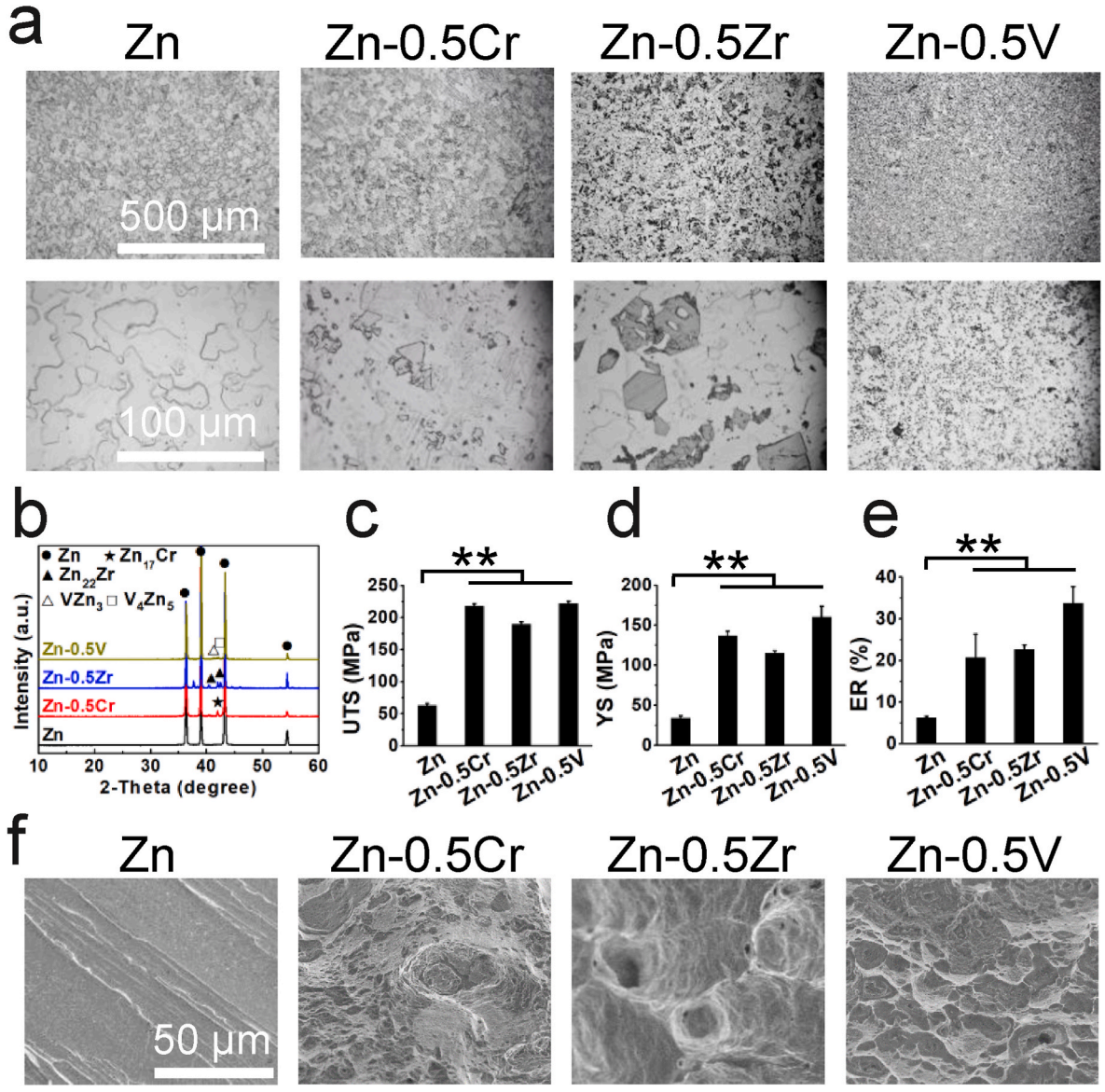

Fig. 1. Microstructure and mechanical property of pure Zn and Zn alloys. (a) Microstructures, (b) XRD patterns, and (c–f) mechanical properties of the as-extruded Zn alloys. (c) Ultimate tensile strength (UTS), (d) yield strength (YS), (e) elongation rate to failure (ER), (f) fracture morphology after tensile test.

significantly improved the mechanical strengths to around 200 MPa (UTS) and 120–160 MPa (YS), while the elongations were also significantly increased to 20–30% simultaneously (Fig. 1c–e). The Zn-0.5 V alloy possessed the best combination of mechanical strength and ductility among all groups. The fracture morphology also indicated similar trends (Fig. 1f). The pure Zn exhibited a smooth fracture surface without obvious plastic deformation, while the Zn alloys showed a quasi-cleavage fracture morphology with numerous cleavage planes. Many dimples appeared on the fracture surface of Zn-0.5 V alloy, indicating its excellent plastic deformation ability.

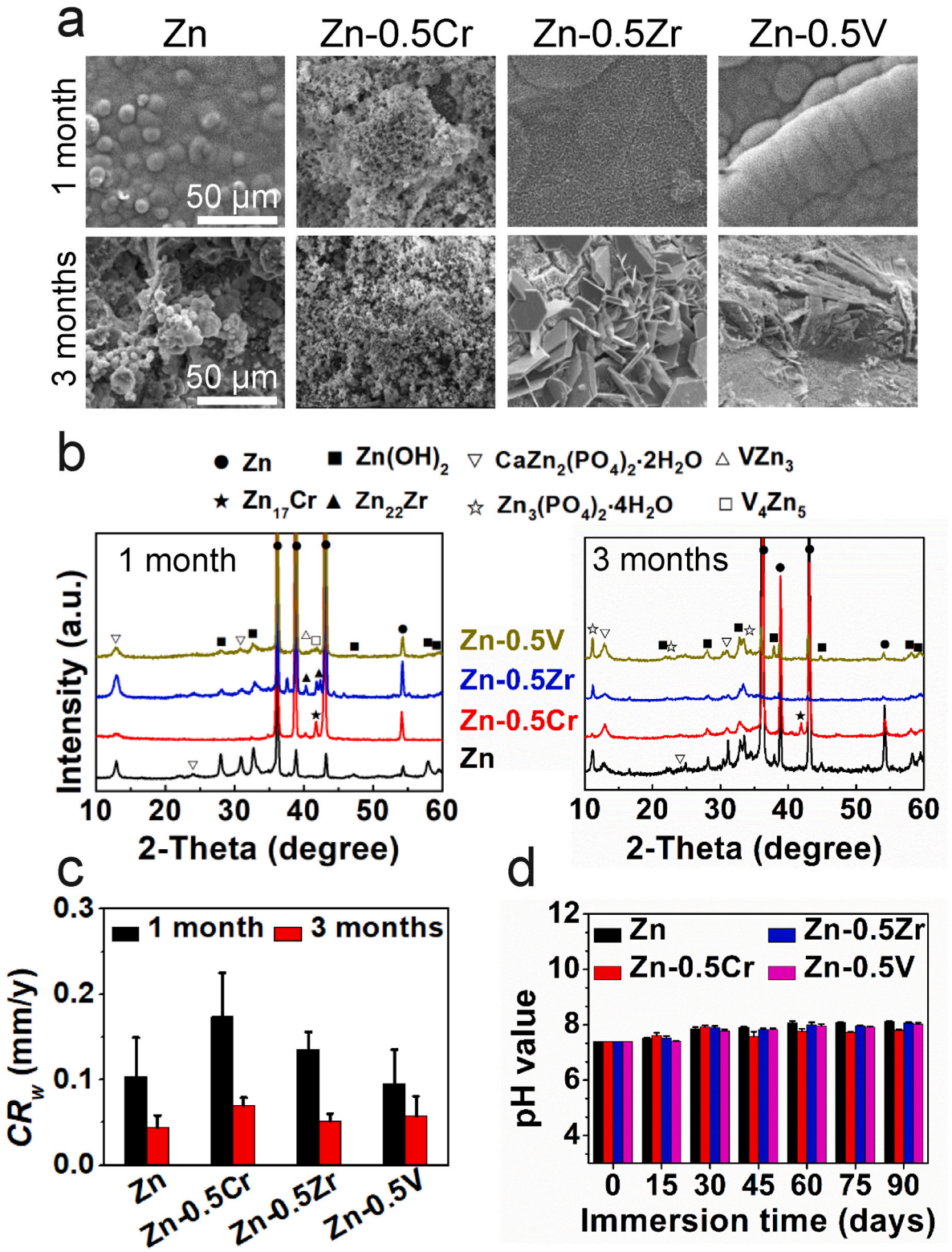

Fig. 2. Degradation behavior of Zn and its alloys in Hank's solution for 1 month and 3 months. (a) Surface morphology, (b) XRD patterns, (c) corrosion rates (CR_w), (d) pH change.

3.2. In vitro degradation behavior

The degradation behaviors were characterized by the degraded morphology, degradation products, corrosion rate, and pH change, as shown in Fig. 2. At one month of immersion, there was similar corrosion product morphology on the pure Zn and Zn-0.5Zr and Zn-0.5 V alloys with the formation of a fine-structured layer made of nanorods clusters, while a porous and cracked corrosion products layer formed on the Zn-0.5Cr surface (Fig. 2a). Correspondingly, the corrosion rate of Zn-0.5Cr was higher than the other groups (Fig. 2c). XRD indicated that the main

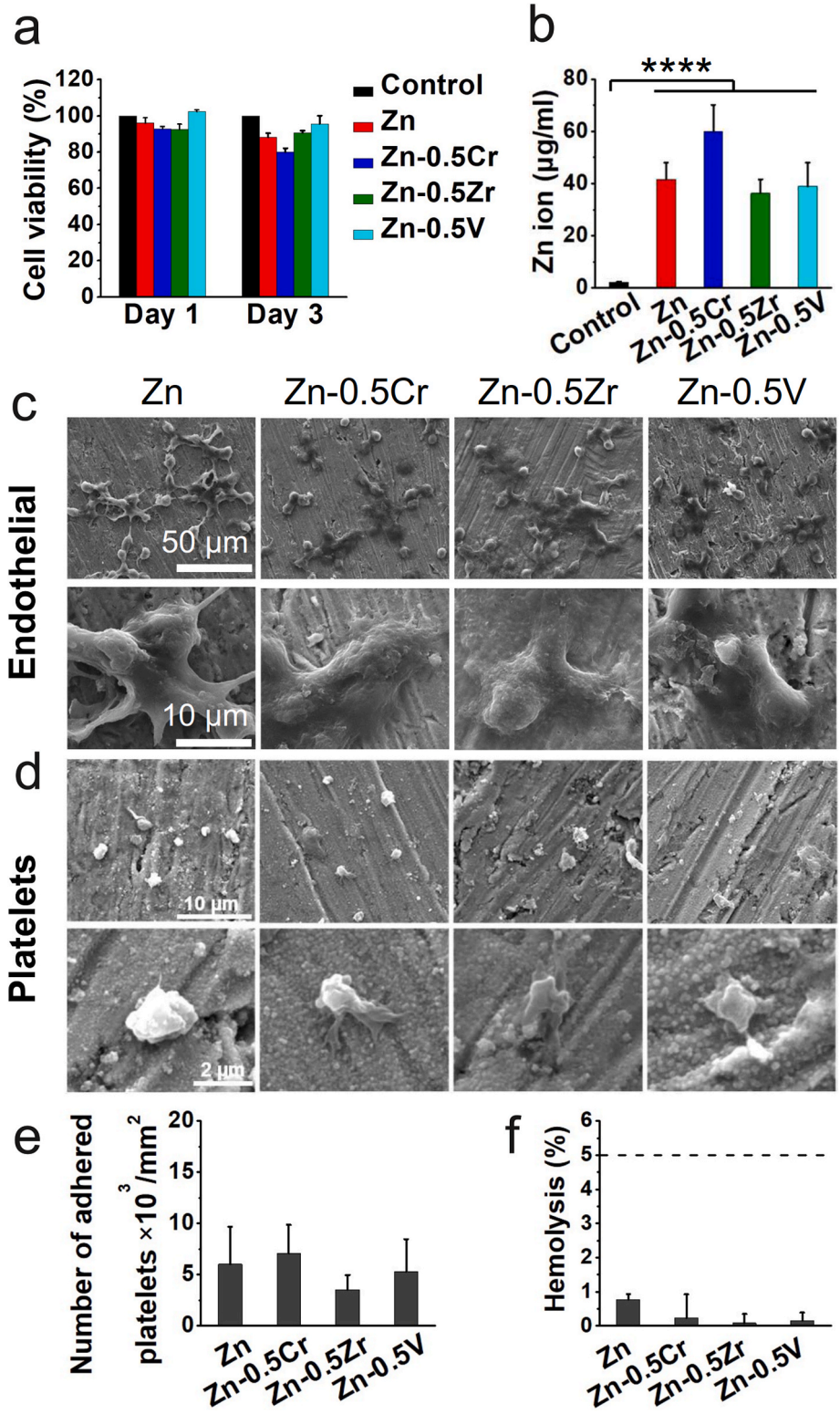

Fig. 3. In vitro biocompatibility of different Zn samples. (a) MTT assay for cell viability of endothelial cell. (b) Zn ion concentration in the corresponding exacts. (c) Endothelial cell adhesion morphology when cultured on Zn samples for 3 days. (d) Platelet adhesion morphology when cultured on Zn samples for 24 h, (e) the corresponding number of adhered platelets, and (f) hemolysis percentage. ****$p < 0.0001$, compared between groups.

degradation products were similar on these samples, which consisted of $Zn(OH)_2$ and $CaZn_2(PO_4)_2{\cdot}2H_2O$ (Fig. 2b). After three months of immersion, the pure Zn and Zn-0.5Cr alloy had severe corrosion morphology with loosely packed corrosion products, but deep corrosion pits were observed on pure Zn (Fig. 2a). There were some flake-like corrosion products formed on the surfaces of Zn-0.5Zr and Zn-0.5 V alloys, which correspond to $Zn_3(PO_4)_2{\cdot}4H_2O$ and $CaZn_2(PO_4)_2{\cdot}2H_2O$ (Fig. 2b). All the samples showed similar corrosion rates and stable pH change during the three months of immersion (Fig. 2c and d).

3.3. In vitro cytocompatibility and hemocompatibility

Endothelial cell viability and adhesion, platelet adhesion, and hemolysis tests were conducted to evaluate the cytocompatibility and hemocompatibility of Zn and its alloys (Fig. 3). The endothelial cells in all Zn alloy groups showed similar cell viability but better attachment and adhesion when compared to pure Zn group (Fig. 3 a and c). The Zn ion releases from all Zn samples were similar due to their similar degradation rates (Fig. 3b). A few adhered platelets were dispersedly distributed on all the Zn surfaces with little spreading (Fig. 3c). The numbers of adhered platelets on all Zn surfaces were similar (Fig. 3d), and their hemolysis rates were also much lower than the hemolysis limit (5%) (Fig. 3e), indicating their good hemocompatibility.

3.4. Antibacterial property

The antibacterial performance of different Zn samples was tested with two bacteria strains *E. coli* and *S. aureus* (Fig. 4). There was a small amount of bacterial adhesion and no biofilm formation on the pure Zn and Zn alloy surfaces, indicating their antiadhesion performance for both bacteria strains. There was much less *S. aureus* adhesion on the pure Zn and Zn-0.5 V surfaces when compared with other groups (Fig. 4a). Compared to the control groups, the antibacterial rate significantly increased to more than 50% for *E. coli* and around 99% for *S. aureus* when cultured with pure Zn and Zn alloys (Fig. 4 b and c). The Zn ion concentrations were measured after 24 h of bacterial culture. There were no significant differences in different Zn groups, although the Zn–Cr group showed slightly higher Zn ion release (Fig. 4 b and c).

3.5. Subcutaneous implantation

Zn and its alloys were first implanted into subcutaneous pockets of rats to evaluate the responses of subcutaneous tissues to the alloys. Micro-CT scanning showed similar morphologies and degradation profiles between Zn, Zn-0.5Zr, and Zn-0.5 V (Fig. 5a and b). However, fractures (arrows in Fig. 5a) and increased degradation could be observed in the Zn-0.5Cr group. Accordingly, macroscopic views of the Zn and the other two alloys showed no noticeable difference after three months of subcutaneous implantation (Fig. 5c), while Zn-0.5Cr broke into two segments (arrows in Fig. 5c). Zn-0.5Cr showed a 5-fold faster degradation rate than the other groups. To evaluate host responses to the implanted alloys, tissues surrounding the alloys were examined with SEM. The SEM images showed a complete cell coverage on the surfaces of all the samples from both axial and cross-section views (Fig. 5d).

To further identify the subcutaneous tissue response and inflammation responses, different histology staining and immunofluorescence staining of CD11b and CD68 were performed (Fig. 6). The H&E staining showed that all the samples were surrounded by an inner layer of necrotic tissues and an outer layer of inflamed tissues. The necrotic tissues were primarily necrotic inflammatory cells and degradation products of the alloys, while the inflamed tissues were mainly living inflammatory cells and fibroblasts. These results indicate parallel host

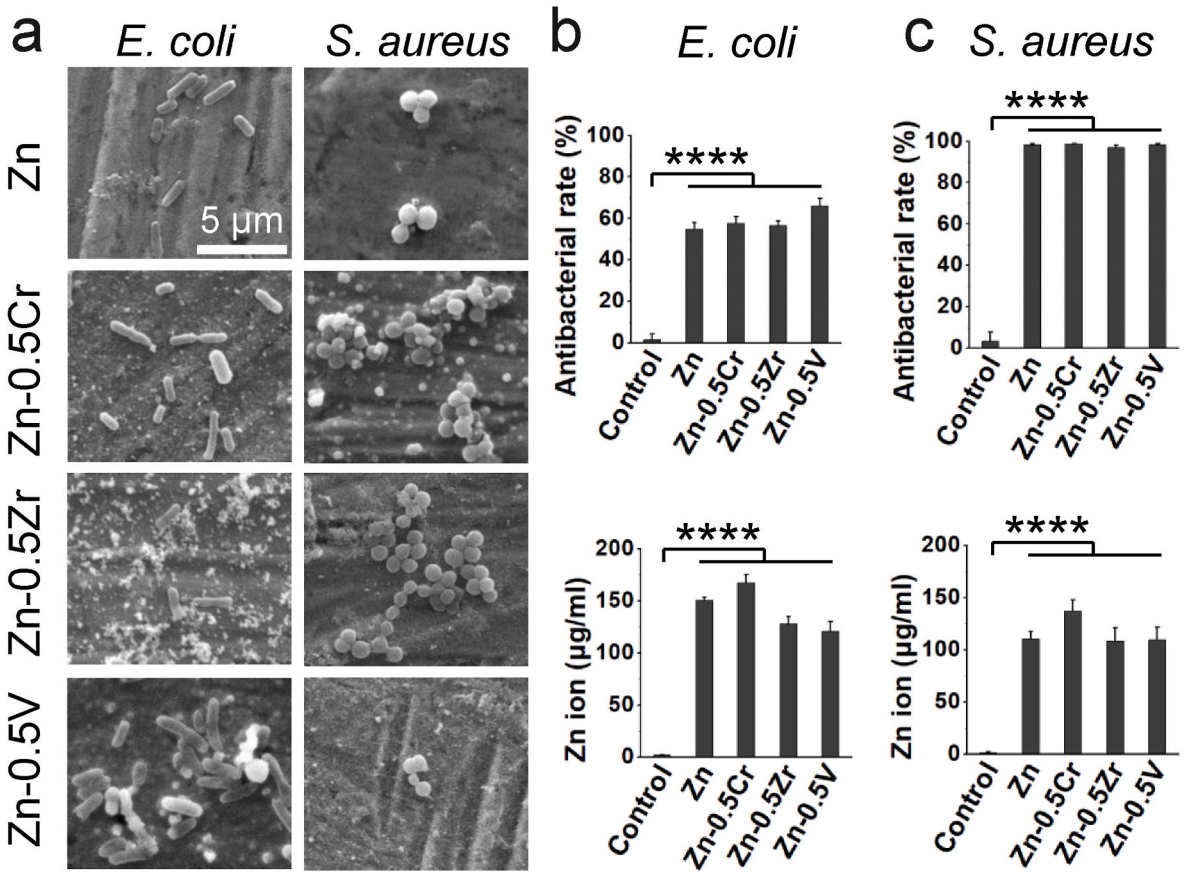

Fig. 4. Antibacterial performance of different Zn surfaces after culture with *E. coli* and *S. aureus* for 24 h. (a) SEM images of bacterial adhesion. Antibacterial rates and corresponding Zn ion concentrations in the culture medium after culture with (b) *E. coli* and (c) *S. aureus*. ****$p < 0.0001$, compared between groups.

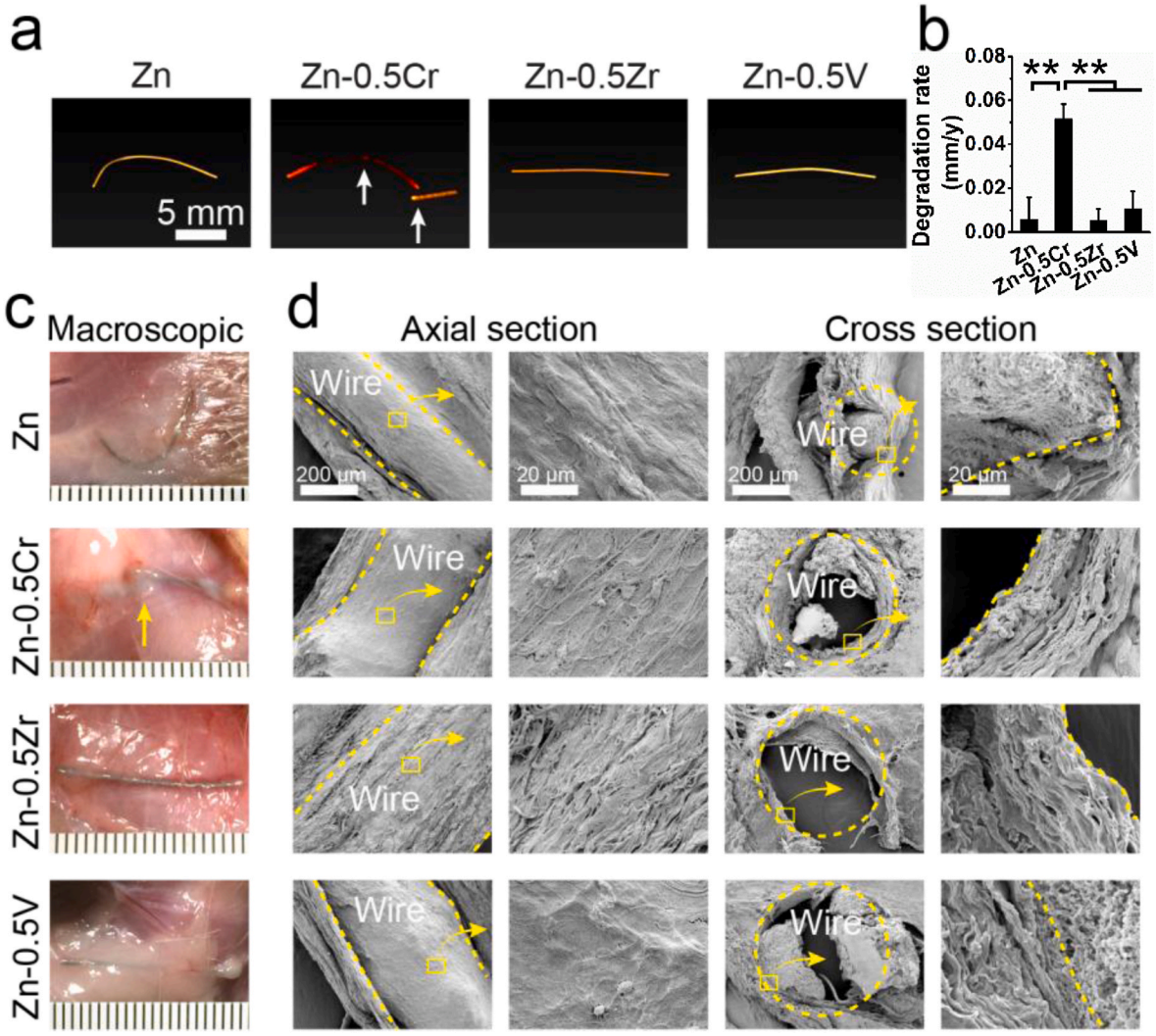

Fig. 5. Subcutaneous implantation of Zn and its alloys in rats after 3 months. (a) CT scanning, (b) *in vivo* degradation profiles, (c) macroscopic views, and (d) SEM images. ** indicates $p < 0.01$, compared between two groups.

responses between Zn and its alloys. However, there was no significant difference in the positively stained cells between Zn and its alloys. Abundant collagen and a thin layer of elastin were observed around all the samples (Fig. 6), which is probably deposited by dermal fibroblasts that can produce extracellular matrix, such as collagen and elastin [48]. CD11b is a marker for pan-white blood cells and is expressed on the surface of monocytes/macrophages, granulocytes, and activated lymphocytes, a subset of NK cells, and a subset of dendritic cells, while CD68 is a monocyte/macrophage-specific marker. $CD11b^{+}$ cells surrounded all the implants. These cells were also positively stained with CD68 (Fig. 6), which suggests monocytes/macrophages are the primary inflammatory cells that participated in alloy degradation under the skin.

3.6. Aortic implantation

Zn and its alloys were further implanted into the abdominal aortas of rats to investigate vascular responses to the alloys. The overall success rate of the surgeries was 100%, and no surgery-associated complications were observed. The implanted alloys could be easily identified through B mode of ultrasound, which presented as white dots above shadows of ultrasound in the abdominal aortas (arrowheads in Fig. 7a). In addition, blood flows in the lumens of the aortas existed all the time, and no occlusion occurred over a 3-month observation window (blue color in Fig. 7a), indicating a good hemocompatibility of the implanted alloys. However, the flow rate in the aortas gradually decreased with time in all the groups, with a significant difference observed only between Zn and Zn-0.5Cr groups in Week 2 (Fig. 7b). The degradation rates were 0.05–0.07 mm/y for all the implants, where the Zn-0.5Cr group still showed the highest value (Fig. 7c). Macroscopic views showed that the two ends of the wires outside of the lumens were wrapped up by fibrotic capsules (Fig. 7d).

The explanted samples were then analyzed by histology. H&E staining showed that the segments of all alloys in the lumens of the aortas were wrapped by neointimas and the quantification data of the neointimal areas showed no significant difference in different groups (Fig. 8a and c). Interfaces between the alloys and the surrounding tissues were clear for Zn, Zn-0.5 V, and Zn-0.5Zr. However, the interfaces between Zn-0.5Cr and the surrounding tissues were blurry with numerous necrotic tissues, which indicates a strong inflammation response (arrows in Fig. 8a). For the segments of the alloys outside of the lumens, metal-vascular matrix interfaces were clear for Zn-0.5 V but a little blurry for Zn, Zn-0.5Zr, and Zn-0.5Cr due to tissue necrosis (arrowheads in Fig. 8b). There were larger inflammation areas surrounding the Zn, Zn-0.5Zr, and Zn-0.5Cr wire implants than that of Zn-0.5 V implant, with the largest inflammation areas observed in Zn-0.5Cr group (Fig. 8d). This result suggests that inflammation induced by Zn-0.5 V is milder than that caused by Zn, Zn-0.5Zr, or Zn-0.5Cr. Besides, the segments of all the alloys in and outside of the lumens were surrounded by collagens

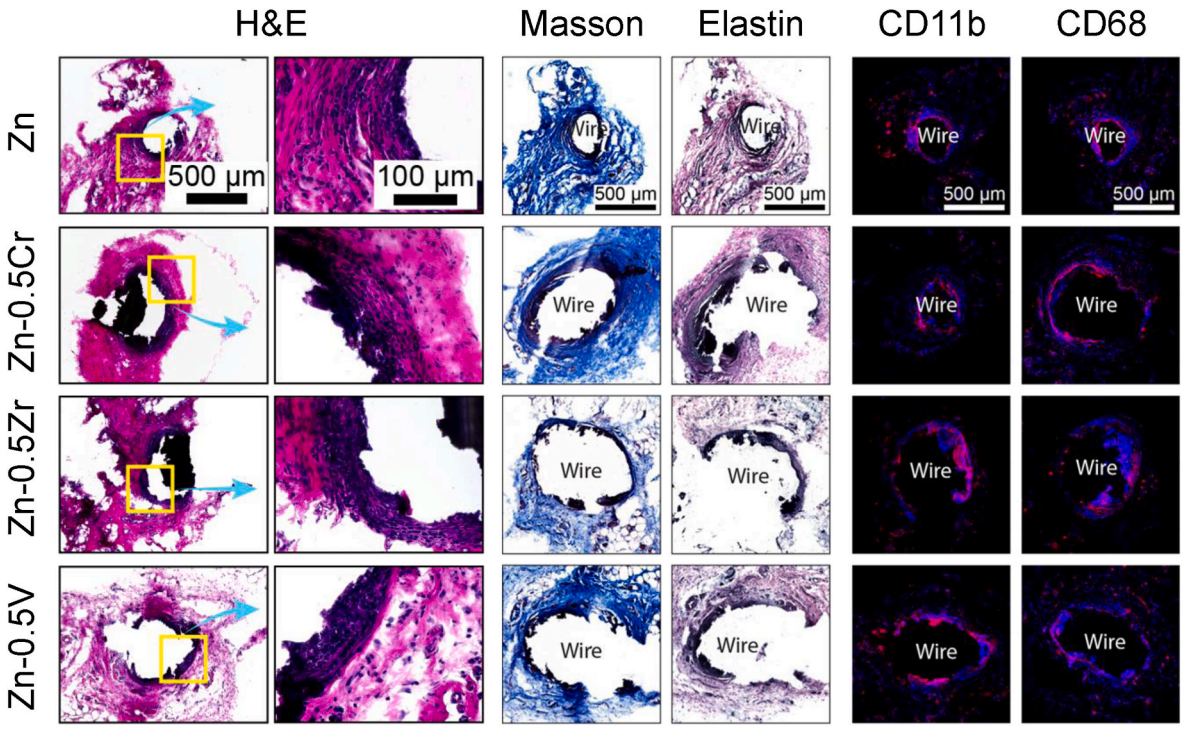

Fig. 6. Staining of Zn and its alloys after 3 months of subcutaneous implantation in rats. H&E, Masson's trichrome, Verhoeff's elastin, and immunofluorescence staining (CD11b and CD68). Blue colors indicate nucleus and red colors indicate positive immunofluorescence staining.

and elastin (Fig. 9 a and b). Fewer collagens were found in Zn-0.5Cr group than those in Zn-0.5Zr and Zn-0.5 V groups, but the elastin contents were similar between different groups (Fig. 9c and d). For the segments of the alloys outside of the lumens, the contents of collagen and elastin were comparable between different groups (Fig. 9e and f).

Monocytes/macrophages were also investigated by immunofluorescence staining (Fig. 10). For segments of the alloys in and outside of lumens, Zn, Zn-0.5Zr, and Zn-0.5 V groups had only a few $CD68^+$ cells and most of them were close to the alloys. However, there were quite a lot of $CD68^+$ cells in the Zn-0.5Cr group (Fig. 10a–c and e), indicating an active inflammation. We further stained samples with CD206, an M2 macrophage marker. Interestingly, for the segments of all the alloys in and outside of lumens, most cells surrounding the alloys were CD206 positive, with a higher percentage in the Zn-0.5Cr group as compared to the pure Zn group (Fig. 10d and f). Since M2 macrophages promote wound healing [49], monocytes/macrophages may differentiate into M2 macrophages, promoting regeneration of the tissues surrounding the alloys. Finally, we evaluated SMC and EC coverage on the surface of the alloys. For the segments of all the alloys in lumens, most cells surrounding the alloys were αSMA positive (Fig. 11a), and the cells in direct contact with the blood were eNOS positive despite some background staining (arrows in Fig. 11a). Larger αSMA positive areas could be observed in the Zn-0.5Cr group (Fig. 11c), while smaller eNOS positive areas were seen in Zn-0.5Cr and Zn-0.5Zr group as compared to pure Zn (Fig. 11d). On the other hand, for the segments of all the alloys outside of lumens, only SMC layers and endothelium of the abdominal aortas were positive for αSMA (Fig. 11b) and eNOS (arrows in Fig. 11b), respectively.

3.7. Femoral implantation

In vivo degradation and hard tissue compatibility were tested for pure Zn and its alloys following 3-month implantation in femur tissue using micro-CT and cross-sectional SEM imaging together with the elemental compositions (Fig. 12). Micro-CT scanning showed similar morphologies and degradation rates (~0.03 mm/y) between Zn, Zn-0.5Zr, and Zn-0.5 V groups, while deep pitting morphology and higher degradation rate (~0.05 mm/y) were observed in the Zn-0.5Cr group (Fig. 12 a-b). The SEM images showed the different gray scales, corresponding to the elemental compositions in EDS mapping. Therefore, the new-formed bone tissue and osteoid tissue were identified together with the implants and the degradation products in the enlarged SEM images. All implants had similar bone formation and osteoid tissue formation surrounding the Zn implants (Fig. 12 d and f). Zn–Cr alloy induced a slightly higher bone formation, which might result from its marginally higher degradation rate when compared to other groups. Zn-0.5Zr alloy showed more degradation products in the cross-sectional images, but it did not induce any significant tissue response. All three Zn alloys induced significantly higher bone-implant contact ratios, indicating the higher bone tissue integration. Masson-Goldner and Elastica van Gieson staining were carried out to further study the femur tissue response with pure Zn and its alloys (Fig. 13). The brick red color in Masson-Goldner staining and the corresponding light red color in Elastin staining are related to the osteoid tissue [50,51]. The identification of the tissues through histological staining confirmed the results in SEM images. New-formed bone tissue was also observed within the osteoid layer (arrows in Fig. 13), indicating the conversion of osteoid tissue to bone tissue.

4. Discussion

4.1. Mechanical improvement

Zn has been regarded as the most promising biodegradable metallic material for biomedical applications, e.g., cardiovascular stents, orthopedic implants, and wound closure devices [5,9,47]. In the exploration for more load-bearing biomedical applications, many alloying elements (Mg, Ca, Sr, Li, Mn, Fe, Cu, and Ag) have been blended to improve the mechanical properties of pure Zn [47]. Among them, only the Mg, Li, Cu, and Ag could stably improve the tensile strength of Zn alloy to over 200 MPa for load-bearing clinical applications [47]. For the first time, the Cr, Zr, and V were provided in the present study as three more alloying

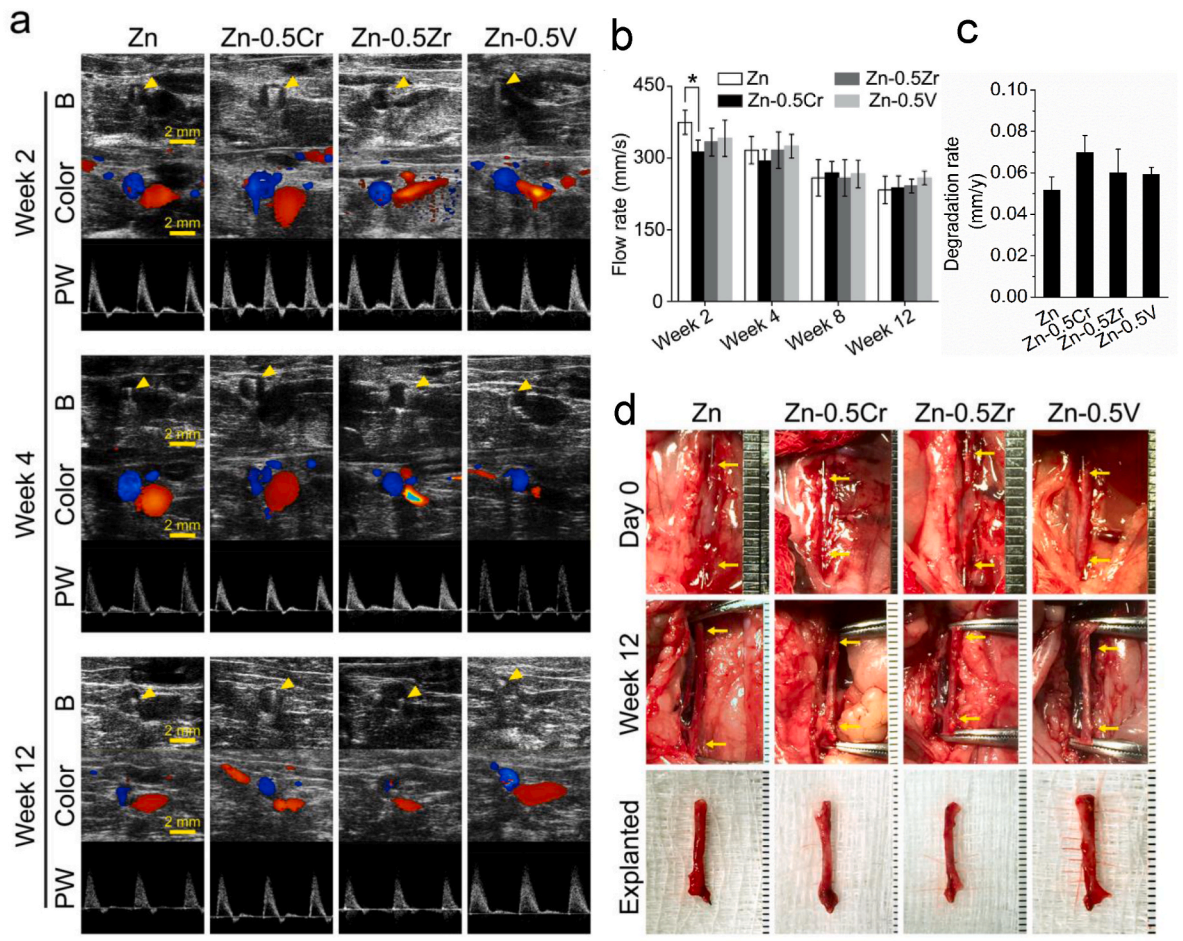

Fig. 7. Abdominal aortas implantation of Zn and its alloys in rats for 3 months. (a) Ultrasound images. Upper: B mode; middle: Doppler mode; Lower: PW mode. Arrow heads indicate the implanted wires within the lumens of the abdominal aortas. (b) Rate of blood flow and (c) degradation rate. * indicates $p < 0.05$, compared between two groups. (d) Macroscopic views of Zn and its alloys in the abdominal aortas upon implantation and 3 months after implantation. Arrows indicate two ends of the implanted Zn and its alloys outside of vessels.

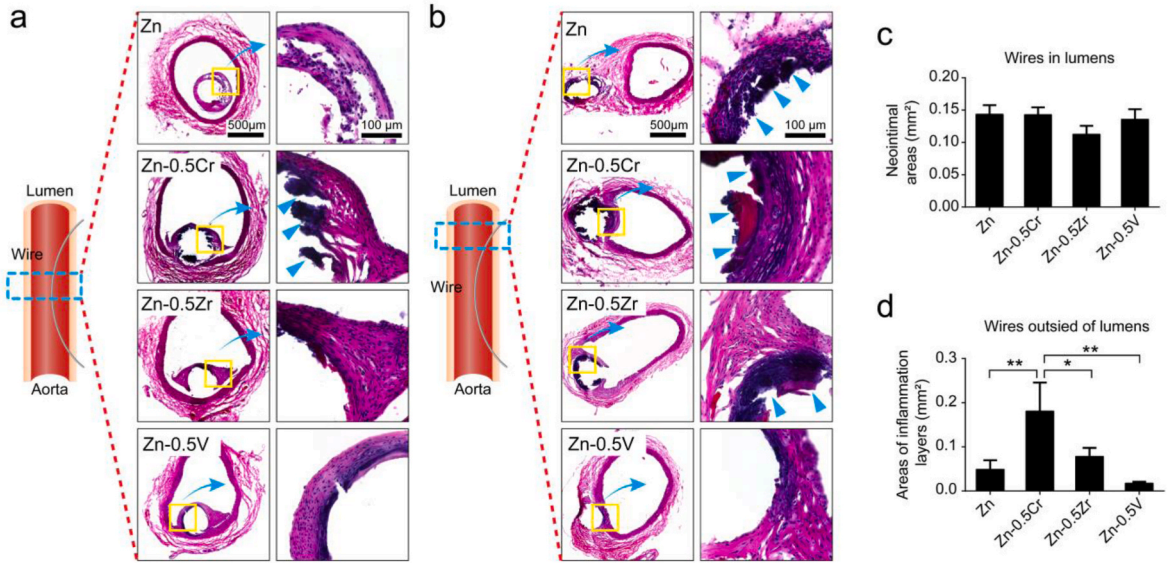

Fig. 8. H&E staining of Zn and its alloys after 3 months of aortic implantation in rats. (a) Wires in lumens. (b) Wires outside of lumens. (c) Quantification of neointimal areas of wires in lumens. (d) Quantification of inflammation layers of wires outside of lumens. Arrow heads indicate necrotic tissues. * indicates $p < 0.05$, ** indicates $p < 0.01$, compared between two groups.

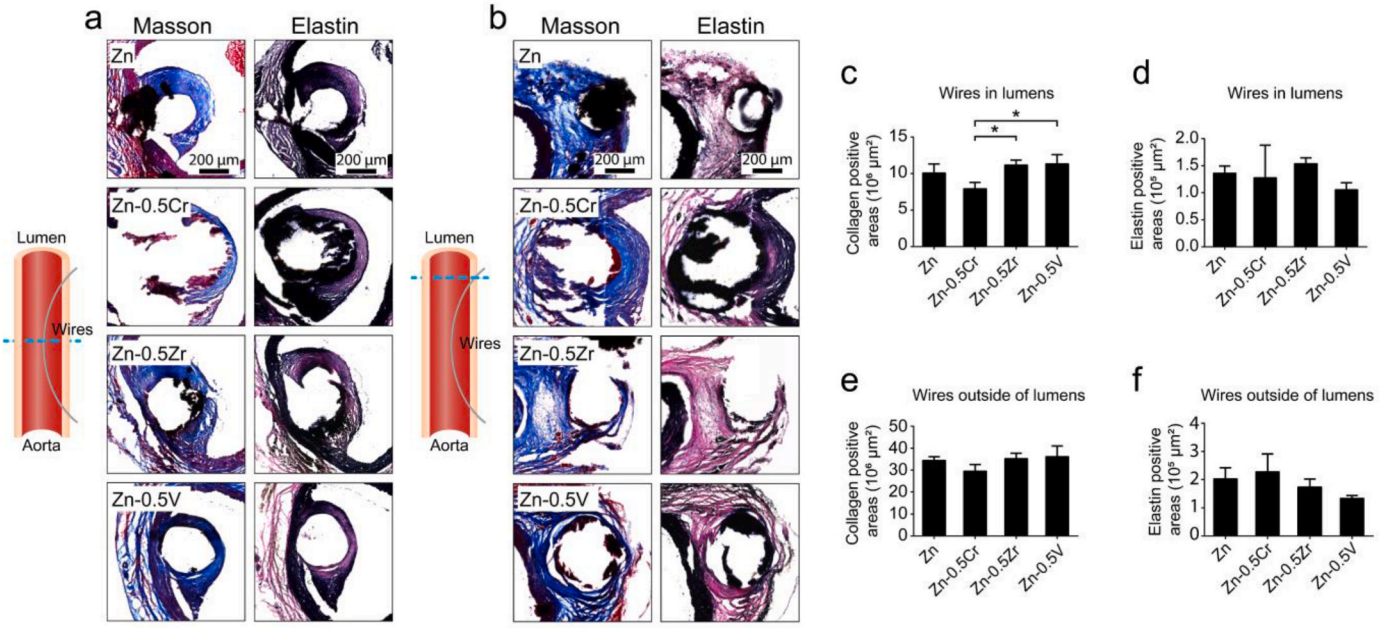

Fig. 9. Masson's trichrome and Verhoeff's elastin staining of Zn and its alloys after 3 months of aortic implantation in rats. (a) Wires in lumens. (b) Wires outside of lumens. Quantification of collagen positive (c) and elastin positive (d) areas of wires in lumens. Quantification of collagen positive (e) and elastin positive (f) areas of wires outside of lumens. * indicates $p < 0.05$, ** indicates $p < 0.01$, compared between two groups.

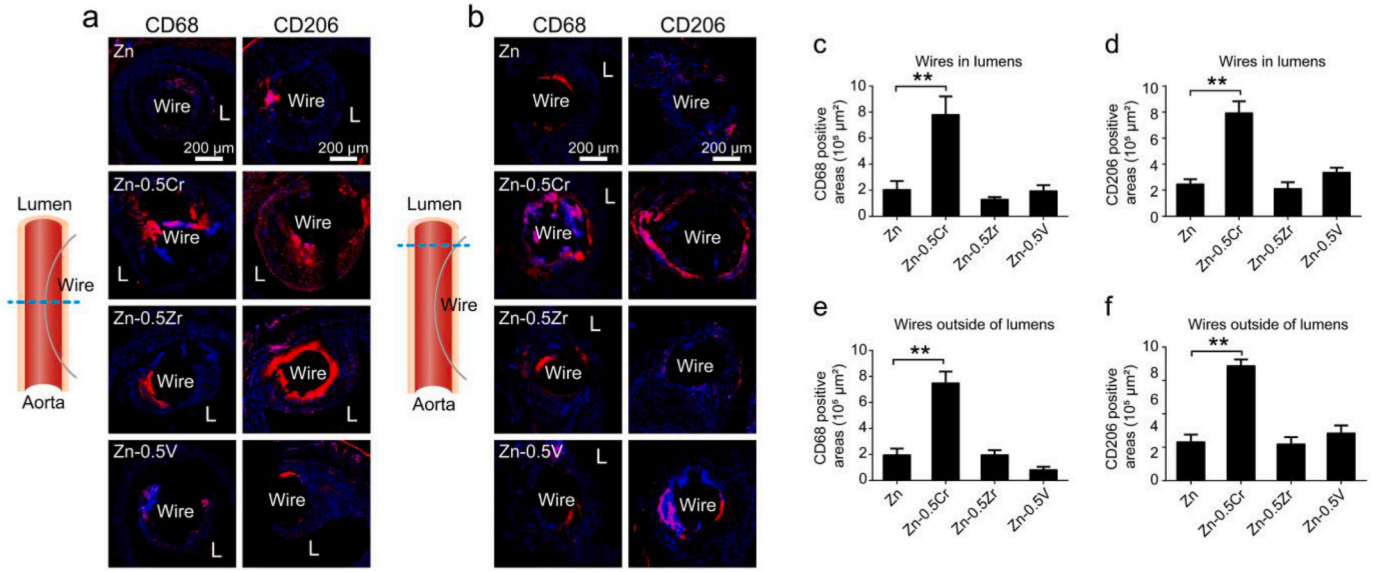

Fig. 10. CD68 and CD206 staining of Zn and its alloys after 3 months of aortic implantation in rats. (a) Wires in lumens. (b) Wires outside of lumens. Quantification of CD68 positive (c) and CD206 positive (d) areas of wires in lumens. Quantification of CD68 positive (e) and CD206 positive (f) areas of wires outside of lumens. * indicates $p < 0.05$, ** indicates $p < 0.01$, compared between two groups. L indicates lumens. Blue colors indicate nucleus and red colors indicate positive staining.

options to improve the tensile strength and elongation to 200 MPa and 20%, respectively (Fig. 1). This mechanical combination enables the fabrication of implants with complex structures [2,47,52]. Moreover, a low amount (0.5%) of alloying elements was screened and chosen due to the low solid solubility of these three elements in Zn. The mechanical strength could be higher after more amount or a third element was added, while the ductility could be diminished [47,53,54].

4.2. *In vitro and in vivo degradation behaviors*

Although the degradation rate of Zn materials has shown to be potentially ideal for many biomedical applications [5,9], the degradation mode is more critical to maintain the mechanical integrity during the degradation process. Compared to the uniform degradation, localized degradation would deteriorate the mechanical integrity and induce the unexpected failure of the load-bearing implants. It has been reported that localized degradation occurred *in vitro* and *in vivo* for pure Zn [1,2,4]. Moreover, localized degradation easily occurs for alloys due to the galvanic coupling between the second phases and the Zn matrix. However, the extrusion treatment could improve the homogenization of the second phase and thus change the precipitation of the degradation products, which could also alter the degradation modes. In the present study, all the Zn alloys presented similar degradation rates *in vitro* (Fig. 2c), but the degradation products differed. The dense-structured

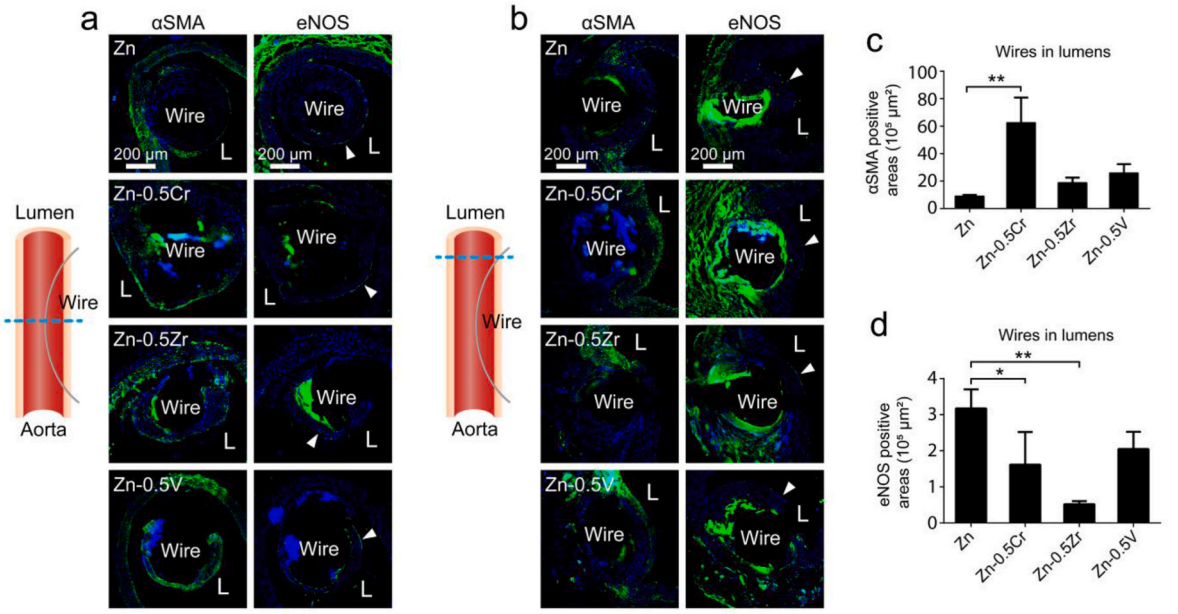

Fig. 11. αSMA and eNOS staining Zn and its alloys after 3 months of aortic implantation in rats. (a) Wires in lumens. (b) Wires outside of lumens. Quantification of αSMA positive (c) and eNOS positive (d) areas of wires in lumens. * indicates $p < 0.05$, ** indicates $p < 0.01$, compared between two groups. Arrow heads indicate endothelium. L indicates lumens. Blue colors indicate nucleus and green colors indicate positive staining.

degradation products made a passive film for the Zn-0.5Zr and Zn-0.5 V alloys, which is helpful to reduce the localized degradation behavior. When compared to Zn-0.5Zr and Zn-0.5 V alloys, there is less intermetallic phase ($Zn_{17}Cr$) in Zn-0.5Cr alloy (Fig. 1a) due to the relatively higher solubility of Cr in Zn [27–29]. The small amount of $Zn_{17}Cr$ could act as an electrochemical couple with Zn substrate and thus induce galvanic corrosion reactions. This could possibly explain why the Zn-0.5Cr possessed loosely packed degradation products.

It is known that the degradation behaviors of biodegradable implants heavily depend on the micro-environment [4,8]. However, the Zn-0.5Cr alloy showed similar degradation rates in both *in vitro* and *in vivo* conditions. The main reason is that the porous degradation products on the Zn-0.5Cr surface could not act as a physical barrier to slow down the corrosion reactions in these conditions. Different from Zn-0.5Cr, pure Zn and the other two Zn alloys showed environment-dependent degradation rates. Compared to the similar degradation rates of around 0.05 mm/y *in vitro* and in aorta vessels (Figs. 2c and 7c), the subcutaneous and femoral tissue degradation rates were much slower, ~0.01 mm/y, and 0.03 mm/y, respectively (Figs. 5b and 12b). Previous studies indicated that the degradation rates were closely relative to the fluid circulation conditions in different implantation locations [55]. Among these *in vivo* scenarios, a thick and dense degradation products film could not be easily formed in the blood vessels due to the stronger blood circulation. In contrast, the dense degradation products film could be easily formed, accumulated, and thickened in the subcutaneous tissue to decrease the degradation reactions, where there is much less fluid circulation. The scenario in femoral tissue is in between that of subcutaneous tissue and blood vessels.

4.3. *In vitro and in vivo biological performances*

Different *in vitro* and *in vivo* models were used to systematically study the biocompatibility of Zn materials. All the Zn materials showed similar *in vitro* cell adhesion and cytocompatibility through the indirect and direct assays (Fig. 3). To target the three main clinical applications: wound closure, cardiovascular stents, and orthopedic implants, three *in vivo* implantation models were explored in rats: subcutaneous, aorta, and femoral implantations. Different host responses to the same kind of Zn alloys implanted in different locations of rats were noticed in this study. For example, Zn-0.5Cr showed a similar inflammation response to pure Zn when implanted subcutaneously (Fig. 6). However, when inserted into the abdominal aortas, quite strong inflammation responses occurred (Figs. 8 and 10). There were more necrotic tissues could be observed around segments of Zn-0.5Cr in lumens of the aortas. The strong inflammation response from Zn-0.5Cr could result from its porous and loose degradation products as well. On the other hand, the Zn-0.5Zr and Zn-0.5 V alloy showed the optimum inflammation responses when implanted in the aortas (Figs. 8 and 10). In addition, collagens and elastin that covered the surface of the alloys implanted subcutaneously were loose (Fig. 6), which were different from the compact structures of collagen and elastin that covered the surface of the alloys in the lumens of the aortas (Fig. 9a). Moreover, SMCs and ECs could be found in regenerated tissues surrounding the alloys in the lumens of the aortas. However, these cells were absent in the regenerated tissues surrounding the wires outside of the vascular walls (Fig. 9a). When implanted in the femoral tissue, all Zn implants were covered by collagens but little elastin. The osteoid layer thickness was quite similar surrounding all the implants, but the contact percentages of the osteoid with pure Zn implant were higher than those of the Zn alloys. This is possibly related to the unstable bone tissue-implant interface due to the more localized degradation behavior of pure Zn (Figs. 2a and 12c) [2]. Therefore, all the Zn alloy implants exhibited higher osseointegration than pure Zn, indicating their improved histocompatibility.

The implantation period of three months is one limitation of this study when evaluating the long-term biological performances of these three biodegradable materials. However, because of the slow degradation rates of the proposed Zn implants, their systemic toxicity is minimal when comparing the ion releasing rates with the respective tolerable upper intake level (UL) values. Specifically, in the present study, the degradation rates in femoral and subcutaneous tissues were much slower than that in the cardiovascular aorta, where the highest degradation rate was ~0.07 mm/y occurred on the Zn-0.5Cr alloy. Considering the entire surface area of a real stent is approximately 100 mm^2 [56], the expected daily release of Zn will be 0.14 mg/day. This is only 1.4% of the recommended daily allowances (RDAs) (~10 mg/day) and far below its UL value for adults (~40 mg/day) [57]. In terms of the three alloying elements studied here, the expected daily release will be lower than 0.8 μg/day, which is also far below their intake values for

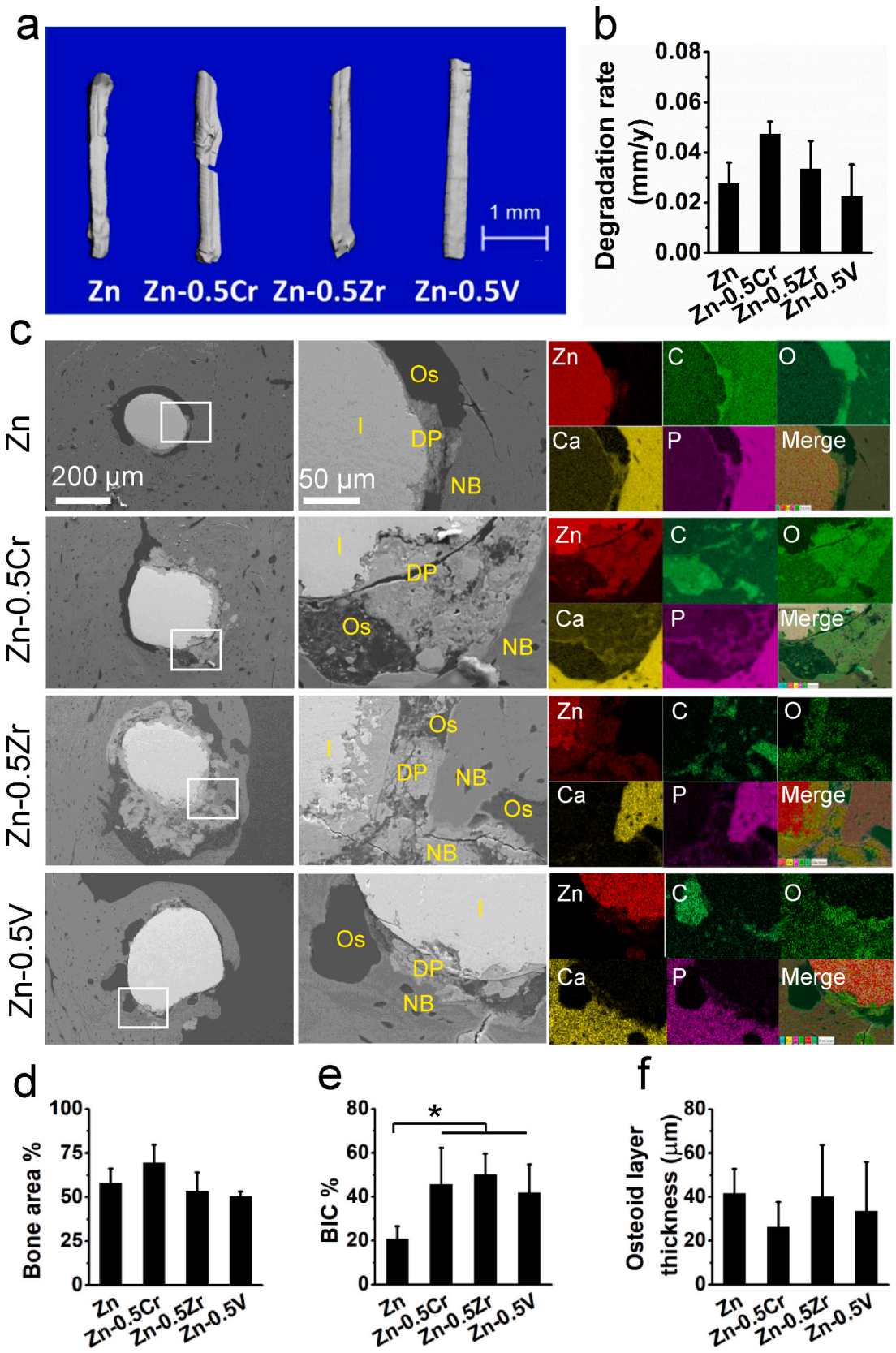

Fig. 12. *In vivo* degradation and bone formation of pure Zn and its alloys when implantation with femur tissue for 3 months. (a) Micro CT scanning, (b) degradation profiles, (c) cross-sectional SEM imaging and EDS mapping, (d) new bone area, (e) bone-implant contact ratio (BIC), and (f) osteoid layer thickness surrounding the implants. I: implants, DP: degradation products, OS: osteoid layer, NB: newborn bone, Zn: zinc, C: carbon, O: oxide, Ca: calcium, P: phosphate.

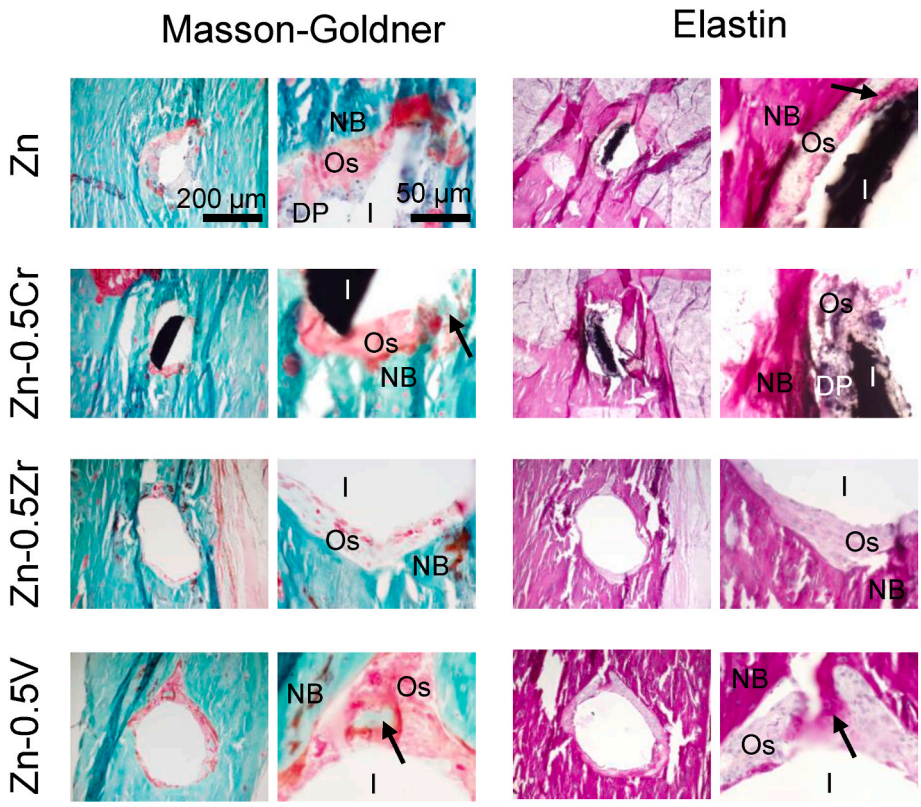

Fig. 13. Masson-Goldner and Elastica van Gieson staining of femur tissue with pure Zn and its alloys implantation for 3 months. I: implants, DP: degradation products, OS: osteoid layer, NB: newborn bone.

adults: RDA value of Cr is 20–35 μg/day, and the average intake levels of Zr and V (are around 4 mg/day and 1.8 mg/day, respectively [57,58]. All three alloying elements together with Zn in such concentration ranges could be considered beneficial. Cr is a micronutrient for mammals and has shown significant biological roles in carbohydrate and lipid metabolism [59,60]. Zr has been blended in the substrate and coating materials for the dental, knee, and hip applications [58,61]. V plays a significant role in cardiovascular and neuronal functions [62,63]. Thus, the Zn implants' systemic toxicity appears not a concern, but a longer-term evolution is still necessary in future clinical applications.

Another limitation of the aortic implantation model is that it cannot replicate the mechanical conditions that a stent is subjected to when deployed in arteries. Due to the size limit of the abdominal aortas in rats (2 mm in diameter), a wire with a 0.2–0.3 mm diameter is preferred for this model [64,65]. However, it only represents a strut of a stent and cannot simulate all aspects of a real stent. For example, it will not be affected by the pulsatile movement of vessels. Thus, following a quick evaluation of degradation behavior and biocompatibility of candidate stent materials in small animals, stent manufacturing and large animal implantation studies are still required.

Antibacterial properties could help prevent biofilm formation and infection during the initial implantation period. As a promising antibacterial agent in biomaterials, Zn could react with bacterial surfaces and result in bacteriolysis during the degradation of Zn materials [6,41,66]. Therefore, all the Zn alloys in this study showed good antiadhesion properties to both bacterial strains (Fig. 4). Although there were no significant differences of Zn ion concentrations in the two bacterial culture media, the antibacterial rate for *E. coli* is around 50%, and that for *S. aureus* is much higher (~99%). This is related to the different surface structures of *E. coli* and *S. aureus*. When compared to *S. aureus*, *E. coli* has an additional outer membrane composed of phospholipids and lipopolysaccharides, facilitating its higher tolerance to the Zn ions and other antibiotic agents [67,68]. Thus, the good antibacterial property of the Zn alloys is another benefit as ideal candidates for biomedical implants.

5. Conclusions

In the exploration of alloying elements for the promising Zn biomaterial, for the first time to our best knowledge, three transmit metal elements, Cr, Zr, V, were used to significantly improve the tensile strength and elongation to 200 MPa and 20%, respectively. The three Zn alloys exhibited more uniform degradation morphology than pure Zn. The Zn-0.5Cr alloy showed similar degradation rates *in vitro* and *in vivo* due to its porous degradation products. Pure Zn and the other two Zn alloys showed environment-dependent degradation rates in the range of 0.01–0.05 mm/y. Although the *in vitro* cell behaviors were similar on all Zn materials, the tissue responses *in vivo* are slightly different and depended on the implantation locations. All Zn implants exhibited similar tissue responses with mild inflammation responses when implanted subcutaneously. Zn-0.5Zr and Zn-0.5 V alloys showed the optimum pro-regenerative inflammation responses in the aorta. All three Zn alloy implants exhibited higher osseointegration than pure Zn. Hence, as biodegradable implant candidates, Zn-0.5Cr, Zn-0.5Zr, and Zn-0.5 V alloys could provide significantly improved mechanical properties and uniform degradation behavior while exhibiting good biocompatibility and antibacterial performance. Although the systemic toxicity of these Zn implants appears not a concern due to the slow degradation rates, a longer-term evolution on large animal models is still necessary in further *in vivo* studies.

Data availability

The data that supports this study is available from the authors upon reasonable request.

Ethics approval and consent to participate

All materials are adhered to high ethical and animal welfare standards. Any use of animals is based on ethological knowledge and respect for species-specific requirements for health and well-being.

All animal procedures were approved by the Cornell University IACUC and Stony Brook University IACUC, following NIH guidelines for the care and use of laboratory animals.

CRediT authorship contribution statement

Yingchao Su: Investigation, Data curation, Writing – original draft. **Jiayin Fu:** Investigation, Data curation, Writing – review & editing. **Juncen Zhou:** Investigation. **Elias Georgas:** Investigation. **Shaokang Du:** Alloying, Investigation. **Yi-Xian Qin:** Resources, Writing – review & editing. **Yadong Wang:** Resources, Writing – review & editing. **Yufeng Zheng:** Resources, Writing – review & editing. **Donghui Zhu:** Resources, Funding acquisition, Writing – review & editing, Supervision.

Declaration of competing interest

All authors declare that they have no conflict of interest.

Acknowledgment

This work was supported by the National Institutes of Health [Grant number R01HL140562 and R01DK129493 to D. Zhu]. The content is solely the responsibility of the authors and does not necessarily represent the official views of the National Institutes of Health.

References

[1] P.K. Bowen, J. Drelich, J. Goldman, Zinc exhibits ideal physiological corrosion behavior for bioabsorbable stents, Adv. Mater. 25 (18) (2013) 2577–2582.
[2] J. Fu, Y. Su, Y.-X. Qin, Y. Zheng, Y. Wang, D. Zhu, Evolution of metallic cardiovascular stent materials: a comparative study among stainless steel, magnesium and zinc, Biomaterials 230 (2020), 119641.
[3] A.S. Prasad, Discovery of human zinc deficiency: its impact on human health and disease, Adv. Nutr. 4 (2) (2013) 176–190.
[4] H. Yang, C. Wang, C. Liu, H. Chen, Y. Wu, J. Han, Z. Jia, W. Lin, D. Zhang, W. Li, W. Yuan, H. Guo, H. Li, G. Yang, D. Kong, D. Zhu, K. Takashima, L. Ruan, J. Nie, X. Li, Y. Zheng, Evolution of the degradation mechanism of pure zinc stent in the one-year study of rabbit abdominal aorta model, Biomaterials 145 (2017) 92–105.
[5] P.K. Bowen, E.R. Shearier, S. Zhao, R.J. Guillory 2nd, F. Zhao, J. Goldman, J. W. Drelich, Biodegradable metals for cardiovascular stents: from clinical concerns to recent Zn-alloys, Adv. Healthc. Mater. 5 (10) (2016) 1121–1140.
[6] Y. Su, I. Cockerill, Y. Wang, Y.X. Qin, L. Chang, Y. Zheng, D. Zhu, Zinc-based biomaterials for regeneration and therapy, Trends Biotechnol. 37 (4) (2019) 428–441.
[7] H.F. Li, X.H. Xie, Y.F. Zheng, Y. Cong, F.Y. Zhou, K.J. Qiu, X. Wang, S.H. Chen, L. Huang, L. Tian, L. Qin, Development of biodegradable Zn-1X binary alloys with nutrient alloying elements Mg, Ca and Sr, Sci. Rep. 5 (2015), 10719.
[8] H. Yang, X. Qu, W. Lin, C. Wang, D. Zhu, K. Dai, Y. Zheng, In vitro and in vivo studies on zinc-hydroxyapatite composites as novel biodegradable metal matrix composite for orthopedic applications, Acta Biomater. 71 (2018) 200–214.
[9] J.M. Seitz, M. Durisin, J. Goldman, J.W. Drelich, Recent advances in biodegradable metals for medical sutures: a critical review, Adv. Healthc. Mater. 4 (13) (2015) 1915–1936.
[10] C. Shen, X. Liu, B. Fan, P. Lan, F. Zhou, X. Li, H. Wang, X. Xiao, L. Li, S. Zhao, Mechanical properties, in vitro degradation behavior, hemocompatibility and cytotoxicity evaluation of Zn-1.2 Mg alloy for biodegradable implants, RSC Adv. 6 (89) (2016) 86410–86419.
[11] H. Gong, K. Wang, R. Strich, J.G. Zhou, In vitro biodegradation behavior, mechanical properties, and cytotoxicity of biodegradable Zn-Mg alloy, J. Biomed. Mater. Res. B Appl. Biomater. 103 (8) (2015) 1632–1640.
[12] N.S. Murni, M.S. Dambatta, S.K. Yeap, G.R.A. Froemming, H. Hermawan, Cytotoxicity evaluation of biodegradable Zn-3Mg alloy toward normal human osteoblast cells, Mater. Sci. Eng. C Mater. Biol. Appl. 49 (2015) 560–566.
[13] M.M. Alves, T. Prošek, C.F. Santos, M.F. Montemor, Evolution of the in vitro degradation of Zn–Mg alloys under simulated physiological conditions, RSC Adv. 7 (45) (2017) 28224–28233.
[14] H.F. Li, H.T. Yang, Y.F. Zheng, F.Y. Zhou, K.J. Qiu, X. Wang, Design and characterizations of novel biodegradable ternary Zn-based alloys with IIA nutrient alloying elements Mg, Ca and Sr, Mater. Des. 83 (2015) 95–102.
[15] X. Liu, J. Sun, Y. Yang, F. Zhou, Z. Pu, L. Li, Y. Zheng, Microstructure, mechanical properties, in vitro degradation behavior and hemocompatibility of novel Zn–Mg–Sr alloys as biodegradable metals, Mater. Lett. 162 (2016) 242–245.
[16] S. Zhao, J.M. Seitz, R. Eifler, H.J. Maier, R.J. Guillory 2nd, E.J. Earley, A. Drelich, J. Goldman, J.W. Drelich, Zn-Li alloy after extrusion and drawing: structural, mechanical characterization, and biodegradation in abdominal aorta of rat, Mater. Sci. Eng. C Mater. Biol. Appl. 76 (2017) 301–312.
[17] Y. Dai, Y. Zhang, H. Liu, H. Fang, D. Li, X. Xu, Y. Yan, L. Chen, Y. Lu, K. Yu, Mechanical strengthening mechanism of Zn-Li alloy and its mini tube as potential absorbable stent material, Mater. Lett. 235 (2019) 220–223.
[18] X. Tong, D. Zhang, X. Zhang, Y. Su, Z. Shi, K. Wang, J. Lin, Y. Li, J. Lin, C. Wen, Microstructure, mechanical properties, biocompatibility, and in vitro corrosion and degradation behavior of a new Zn-5Ge alloy for biodegradable implant materials, Acta Biomater. 82 (2018) 197–204.
[19] X. Tong, D. Zhang, J. Lin, Y. Dai, Y. Luan, Q. Sun, Z. Shi, K. Wang, Y. Gao, J. Lin, Development of biodegradable Zn–1Mg–0.1 RE (RE= Er, Dy, and Ho) alloys for biomedical applications, Acta Biomater. 117 (2020) 384–399.
[20] Q.Z. Chen, G.A. Thouas, Metallic implant biomaterials, Mater. Sci. Eng. R Rep. 87 (2015) 1–57.
[21] Z.Z. Shi, J. Yu, X.F. Liu, H.J. Zhang, D.W. Zhang, Y.X. Yin, L.N. Wang, Effects of Ag, Cu or Ca addition on microstructure and comprehensive properties of biodegradable Zn-0.8Mn alloy, Mater. Sci. Eng. C 99 (2019) 969–978.
[22] M. Sikora-Jasinska, E. Mostaed, A. Mostaed, R. Beanland, D. Mantovani, M. Vedani, Fabrication, mechanical properties and in vitro degradation behavior of newly developed Zn-Ag alloys for degradable implant applications, Mat. Sci. Eng. C-Mater. 77 (2017) 1170–1181.
[23] A. Kafri, S. Ovadia, G. Yosafovich-Doitch, E. Aghion, The effects of 4%Fe on the performance of pure zinc as biodegradable implant material, Ann. Biomed. Eng. 47 (6) (2019) 1400–1408.
[24] X. Tong, Z. Shi, L. Xu, J. Lin, D. Zhang, K. Wang, Y. Li, C. Wen, Degradation behavior, cytotoxicity, hemolysis, and antibacterial properties of electro-deposited Zn–Cu metal foams as potential biodegradable bone implants, Acta Biomater. 102 (2019) 481–492.
[25] J. Niu, Z. Tang, H. Huang, J. Pei, H. Zhang, G. Yuan, W. Ding, Research on a Zn-Cu alloy as a biodegradable material for potential vascular stents application, Mater. Sci. Eng. C Mater. Biol. Appl. 69 (2016) 407–413.
[26] Z. Tang, H. Huang, J. Niu, L. Zhang, H. Zhang, J. Pei, J. Tan, G. Yuan, Design and characterizations of novel biodegradable Zn-Cu-Mg alloys for potential biodegradable implants, Mater. Des. 117 (2017) 84–94.
[27] H. Okamoto, Cr-Zn (Chromium-Zinc), J. Phase Equilibria Diffus. 33 (3) (2012) 246–247.
[28] H. Okamoto, Zn-Zr (zinc-zirconium), J. Phase Equilibria Diffus. 28 (2) (2007) 236–237.
[29] H. Okamoto, V-Zn (Vanadium-Zinc), J. Phase Equilibria Diffus. 32 (3) (2011), 259-259.
[30] C. Chen, J. Niu, H. Huang, D. Zhu, J.-F. Nie, G. Yuan, Basal-plane stacking fault energies of biodegradable Zn-based alloys: a first-principles study of alloying effects, Mater. Lett. 309 (2022), 131413.
[31] Y. Liu, Y. Zheng, X.-H. Chen, J.-A. Yang, H. Pan, D. Chen, L. Wang, J. Zhang, D. Zhu, S. Wu, K.W.K. Yeung, R.-C. Zeng, Y. Han, S. Guan, Fundamental theory of biodegradable metals-definition, criteria, and design, Adv. Funct. Mater. 29 (18) (2019), 1805402.
[32] A.J. Drelich, P.K. Bowen, L. LaLonde, J. Goldman, J.W. Drelich, Importance of oxide film in endovascular biodegradable zinc stents, Surf. Innov. 4 (3) (2016) 133–140.
[33] A.A.S.f. Testing, Materials, Standard Test Methods for Tension Testing of Metallic Materials, ASTM international, 2009.
[34] J. Levesque, H. Hermawan, D. Dube, D. Mantovani, Design of a pseudo-physiological test bench specific to the development of biodegradable metallic biomaterials, Acta Biomater. 4 (2) (2008) 284–295.
[35] Y. Su, S. Champagne, A. Trenggono, R. Tolouei, D. Mantovani, H. Hermawan, Development and characterization of silver containing calcium phosphate coatings on pure iron foam intended for bone scaffold applications, Mater. Des. 148 (2018) 124–134.
[36] Z.M. Shi, A. Atrens, An innovative specimen configuration for the study of Mg corrosion, Corrosion Sci. 53 (1) (2011) 226–246.
[37] Y. Su, G. Li, J. Lian, A chemical conversion hydroxyapatite coating on AZ60 magnesium alloy and its electrochemical corrosion behaviour, Int. J. Electrochem. Sci. 7 (11) (2012) 11497–11511.
[38] A. G31-12a, Standard Guide for Laboratory Immersion Corrosion Testing of Metals, ASTM West, Conshohocken, PA, 2012.
[39] X. Gu, Y. Zheng, Y. Cheng, S. Zhong, T. Xi, In vitro corrosion and biocompatibility of binary magnesium alloys, Biomaterials 30 (4) (2009) 484–498.
[40] S. Hauser, F. Jung, J. Pietzsch, Human endothelial cell models in biomaterial research, Trends Biotechnol. 35 (3) (2017) 265–277.
[41] Y. Su, K. Wang, J. Gao, Y. Yang, Y.X. Qin, Y. Zheng, D. Zhu, Enhanced cytocompatibility and antibacterial property of zinc phosphate coating on biodegradable zinc materials, Acta Biomater. 98 (2019) 174–185.
[42] J. Fischer, D. Pröfrock, N. Hort, R. Willumeit, F. Feyerabend, Improved cytotoxicity testing of magnesium materials, Mater. Sci. Eng., B 176 (11) (2011) 830–834.
[43] J. Wang, F. Witte, T. Xi, Y. Zheng, K. Yang, Y. Yang, D. Zhao, J. Meng, Y. Li, W. Li, K. Chan, L. Qin, Recommendation for modifying current cytotoxicity testing standards for biodegradable magnesium-based materials, Acta Biomater. 21 (2015) 237–249.

[44] D.A. Robinson, R.W. Griffith, D. Shechtman, R.B. Evans, M.G. Conzemius, In vitro antibacterial properties of magnesium metal against Escherichia coli, Pseudomonas aeruginosa and Staphylococcus aureus, Acta Biomater. 6 (5) (2010) 1869–1877.
[45] Y. Jang, Z. Tan, C. Jurey, Z. Xu, Z. Dong, B. Collins, Y. Yun, J. Sankar, Understanding corrosion behavior of Mg-Zn-Ca alloys from subcutaneous mouse model: effect of Zn element concentration and plasma electrolytic oxidation, Mater. Sci. Eng. C Mater. Biol. Appl. 48 (2015) 28–40.
[46] F. Peng, H. Li, D. Wang, P. Tian, Y. Tian, G. Yuan, D. Xu, X. Liu, Enhanced corrosion resistance and biocompatibility of magnesium alloy by Mg-Al-layered double hydroxide, ACS Appl. Mater. Interfaces 8 (51) (2016) 35033–35044.
[47] H. Yang, B. Jia, Z. Zhang, X. Qu, G. Li, W. Lin, D. Zhu, K. Dai, Y. Zheng, Alloying design of biodegradable zinc as promising bone implants for load-bearing applications, Nat. Commun. 11 (1) (2020) 401.
[48] S.J. Hwang, G.-H. Ha, W.-Y. Seo, C.K. Kim, K. Kim, S.B. Lee, Human collagen alpha-2 type I stimulates collagen synthesis, wound healing, and elastin production in normal human dermal fibroblasts (HDFs), BMB Rep. 53 (10) (2020) 539.
[49] D.M. Mosser, J.P. Edwards, Exploring the full spectrum of macrophage activation, Nat. Rev. Immunol. 8 (12) (2008) 958–969.
[50] N. Fratzl-Zelman, I. Schmidt, P. Roschger, A. Roschger, F.H. Glorieux, K. Klaushofer, W. Wagermaier, F. Rauch, P. Fratzl, Unique micro-and nano-scale mineralization pattern of human osteogenesis imperfecta type VI bone, Bone 73 (2015) 233–241.
[51] F.H. Glorieux, L.M. Ward, F. Rauch, L. Lalic, P.J. Roughley, R. Travers, Osteogenesis imperfecta type VI: a form of brittle bone disease with a mineralization defect, J. Bone Miner. Res. 17 (1) (2002) 30–38.
[52] G. Li, H. Yang, Y. Zheng, X.H. Chen, J.A. Yang, D. Zhu, L. Ruan, K. Takashima, Challenges in the use of zinc and its alloys as biodegradable metals: perspective from biomechanical compatibility, Acta Biomater. 97 (2019) 23–45.
[53] J. Kubasek, D. Vojtech, E. Jablonska, I. Pospisilova, J. Lipov, T. Ruml, Structure, mechanical characteristics and in vitro degradation, cytotoxicity, genotoxicity and mutagenicity of novel biodegradable Zn-Mg alloys, Mater. Sci. Eng. C Mater. Biol. Appl. 58 (2016) 24–35.
[54] D. Vojtech, J. Kubasek, J. Serak, P. Novak, Mechanical and corrosion properties of newly developed biodegradable Zn-based alloys for bone fixation, Acta Biomater. 7 (9) (2011) 3515–3522.
[55] Y. Su, H. Yang, J. Gao, Y.X. Qin, Y. Zheng, D. Zhu, Interfacial zinc phosphate is the key to controlling biocompatibility of metallic zinc implants, Adv. Sci. 6 (14) (2019), 1900112.
[56] M. Saqib, R. Bernhardt, M. Kästner, N. Beshchasna, G. Cuniberti, J. Opitz, Determination of the entire stent surface area by a new analytical method, Materials 13 (24) (2020) 5633.
[57] P. Trumbo, A.A. Yates, S. Schlicker, M. Poos, Dietary reference intakes: vitamin A, vitamin K, arsenic, boron, chromium, copper, iodine, iron, manganese, molybdenum, nickel, silicon, vanadium, and zinc, J. Am. Diet Assoc. 101 (3) (2001) 294–301.
[58] D.B. Lee, M. Roberts, C.G. Bluchel, R.A. Odell, Zirconium: biomedical and nephrological applications, Am. Soc. Artif. Intern. Organs J. 56 (6) (2010) 550–556.
[59] J.B. Vincent, The biochemistry of chromium, J. Nutr. 130 (4) (2000) 715–718.
[60] J.B. Vincent, Elucidating a biological role for chromium at a molecular level, Acc. Chem. Res. 33 (7) (2000) 503–510.
[61] A.G. Sanchez, W. Schreiner, G. Duffó, S. Ceré, Surface characterization of anodized zirconium for biomedical applications, Appl. Surf. Sci. 257 (15) (2011) 6397–6405.
[62] D. Rehder, The role of vanadium in biology, Metallomics 7 (5) (2015) 730–742.
[63] R.J. French, P.J. Jones, Role of vanadium in nutrition: metabolism, essentiality and dietary considerations, Life Sci. 52 (4) (1993) 339–346.
[64] P.K. Bowen, R.J. Guillory 2nd, E.R. Shearier, J.M. Seitz, J. Drelich, M. Bocks, F. Zhao, J. Goldman, Metallic zinc exhibits optimal biocompatibility for bioabsorbable endovascular stents, Mater. Sci. Eng. C Mater. Biol. Appl. 56 (2015) 467–472.
[65] D. Pierson, J. Edick, A. Tauscher, E. Pokorney, P. Bowen, J. Gelbaugh, J. Stinson, H. Getty, C.H. Lee, J. Drelich, J. Goldman, A simplified in vivo approach for evaluating the bioabsorbable behavior of candidate stent materials, J. Biomed. Mater. Res. B Appl. Biomater. 100 (1) (2012) 58–67.
[66] Y.W. Wang, A. Cao, Y. Jiang, X. Zhang, J.H. Liu, Y. Liu, H. Wang, Superior antibacterial activity of zinc oxide/graphene oxide composites originating from high zinc concentration localized around bacteria, ACS Appl. Mater. Interfaces 6 (4) (2014) 2791–2798.
[67] Q.L. Feng, J. Wu, G. Chen, F. Cui, T. Kim, J. Kim, A mechanistic study of the antibacterial effect of silver ions on Escherichia coli and Staphylococcus aureus, J. Biomed. Mater. Res. 52 (4) (2000) 662–668.
[68] M. Yasuyuki, K. Kunihiro, S. Kurissery, N. Kanavillil, Y. Sato, Y. Kikuchi, Antibacterial properties of nine pure metals: a laboratory study using Staphylococcus aureus and Escherichia coli, Biofouling 26 (7) (2010) 851–858.